Warm Arctic-Cold Eurasia Pattern Driven by Atmospheric Blocking in Models and Observations

Zachary Kaufman (zackkauf@stanford.edu)[a,b]*, Nicole Feld (nfeldl@ucsc.edu)l[b], Claudie Beaulieu (beaulieu@ucsc.edu)[c]

[a]Earth System Science Department, Stanford University

[b]Earth and Planetary Science Department, University of California, Santa Cruz

[c]Ocean Science Department, University of California, Santa Cruz

Peer-review statement
This manuscript preprint has been submitted to *Environmental Research: Climate* and is not peer-reviewed.

Warm Arctic-Cold Eurasia Pattern Driven by Atmospheric Blocking in Models and Observations

Zachary Kaufman[1,2], **Nicole Feldl**[2], **and Claudie Beaulieu**[3]

[1] Earth System Science Department, Stanford University

[2] Earth and Planetary Science Department, University of California, Santa Cruz

[3] Ocean Science Department, University of California, Santa Cruz

E-mail: `zackkauf@stanford.edu`

Abstract. In recent decades, Arctic-amplified warming and sea-ice loss coincided with a prolonged wintertime Eurasian cooling trend. This observed Warm Arctic-Cold Eurasia pattern has often been attributed to sea-ice forced changes in the midlatitude atmospheric circulation, implying an anthropogenic cause. However, comprehensive climate change simulations do not produce Eurasian cooling, instead suggesting a role for unforced atmospheric variability. This study seeks to clarify the source of this model-observation discrepancy by developing a statistical approach that enables direct comparison of Arctic-midlatitude interactions. In both historical simulations and observations, we first identify Ural blocking as the primary causal driver of sea ice, temperature, and circulation anomalies consistent with the Warm Arctic-Cold Eurasia pattern. Next, we quantify distinct transient responses to this Ural blocking, which explain the model-observation discrepancy in historical Eurasian temperature. Observed 1988-2012 Eurasian cooling occurs in response to a pronounced positive trend in Ural sea-level pressure, temporarily masking long-term midlatitude warming. This observed sea-level pressure trend lies beyond the outer edge of simulated variability in a fully coupled large ensemble, where smaller sea-level pressure trends have little impact on the ensemble mean temperature trend over Eurasia. Accounting for these differences bring observed and simulated trends into remarkable agreement. Finally, we quantify the influence of sea-ice loss on the magnitude of the observed Ural sea-level pressure trend, an effect that is absent in historical simulations. These results illustrate that sea-ice loss and tropospheric variability can both play a role in producing Eurasian cooling. Furthermore, by conducting a direct model-observation comparison, we reveal a key difference in the causal structures characterizing the Warm Arctic-Cold Eurasia Pattern, which will guide ongoing efforts to explain the lack of Eurasian cooling in climate change simulations.

Submitted to: *Environ. Res.: Clim.*

1. Introduction

Arctic sea-ice loss is one of the most dramatic manifestations of global climate change in the observational satellite record (Masson-Delmotte et al. 2021), and concurrent

Arctic near-surface warming trends have outpaced the global average (Taylor et al. 2021). Surprisingly, Arctic-amplified warming and sea-ice loss also coincided with a multi-decade wintertime cooling trend over midlatitude continents, especially between 1988-2012 (Cohen et al. 2012; Overland et al. 2015; Outten et al. 2023). While the midlatitude cooling trend has abated in recent years (Blackport and Screen 2020), strong patterns of co-variability between Arctic sea-ice extent and midlatitude surface temperature remain a notable feature of the climate system (Cohen et al. 2021). This observed covariance has motivated the search for dynamical mechanisms that link Arctic warming and midlatitude cooling, whereby decreases in sea-ice extent drive changes in extratropical atmospheric circulation.

The clearest regional signature of this Arctic-midlatitude linkage involves negative sea-ice anomalies in the Barents-Kara Sea and cold surface temperature anomalies over Eurasia, which are typically accompanied by anticyclonic circulation anomalies over the Ural Mountains (Luo et al. 2016; Mori et al. 2019). Together, these metrics represent the Warm Arctic-Cold Eurasia pattern, the primary focus of this study. In the region, a range of relevant mechanisms have been proposed as evidence that sea-ice forced changes in atmospheric circulation cool the midlatitudes. Proposed processes include weakening of the stratospheric polar vortex by vertical wave fluxes over regions of sea-ice loss (Kim et al. 2014), weakening of thermal wind by a reduced equator-to-pole temperature gradient (Yao et al. 2017), disruptions in tropospheric zonal-mean zonal wind by planetary-scale Rossby waves (Honda et al. 2009; Francis and Vavrus 2012; Francis and Vavrus 2015), and the alteration of meridional potential vorticity gradients (Luo et al. 2018; Luo et al. 2019; Xie et al. 2020). However, atmospheric circulation variability (most notably, Ural blocking) has also been shown to independently drive both Eurasian temperature and sea-ice anomalies, highlighted in both observation-based studies (Gong and Luo 2017; Luo et al. 2017; Sorokina et al. 2016; Tyrlis et al. 2019) and model experiments (Peings 2019; Liu et al. 2022). Accordingly, the chain of causality among the co-varying regional anomalies remains unclear, and studies-to-date remain divided on the existence and strength of a forced response to sea-ice loss (Barnes and Screen 2015; Cohen et al. 2020).

The source of the Warm Arctic-Cold Eurasia Pattern is further obscured by apparent discrepancies between climate models and observations. Fully coupled climate change simulations generally show weak midlatitude responses to sea-ice loss and are unable to reproduce the observed prolonged period of historical Eurasian cooling (Sun et al. 2016; Boland et al. 2017; Ogawa et al. 2018). This model-observation discrepancy has been attributed to internal climate variability (Blackport and Screen 2021), as well as to systematic underestimates by models of the variability in Eurasian temperatures associated with sea ice loss (Mori et al. 2019; Smith et al. 2022). From a probabilistic viewpoint, these explanations need not be mutually exclusive; anthropogenic sea-ice loss and internal variability can both be important factors that affect the likelihood of prolonged Eurasian cooling (Outten et al. 2023).

Beyond simulations from freely running coupled models, targeted perturbation experiments can be used to isolate midlatitude responses to sea-ice loss. Yet, the results of these experiments are highly dependent on study design, such as the location of prescribed sea-ice loss (i.e, pan-Arctic vs. regional; Nishii et al. 2011; Screen 2017), inclusion of a dynamic ocean (Deser et al. 2016), or the vertical resolution of the climate model being used, which may impact stratosphere-troposphere coupling (Sun et al. 2015). Separating the forced response to Arctic climate change from internal variability also requires simulating many ensemble members, which entails high computational costs (Liang et al. 2020; Peings et al. 2021). Most importantly, observational studies are constrained by the relatively short length of the reliable satellite record, and empirical evaluations of these observations often lack attributions of causality that could be compared with climate model experiments (Liang et al. 2021).

This study seeks to identify and quantify causal pathways in the Warm Arctic-Cold Eurasia Pattern. To achieve this goal, we use a statistical causal inference method (Runge et al. 2019), which has enabled more robust quantification of two-way Arctic-midlatitude interactions in recent observational studies (Kretschmer et al. 2016; Siew et al. 2020). To address challenges of model-observation discrepancy, we expand this technique's application with a like-for-like comparison of causal effects, inferred separately, for both observations and model output, which has yet to be conducted. We additionally support our causal effect quantification with linear convolution theory, which isolates the transient climate response to the time history of midlatitude circulation in each data source. Our flexible approach thus resolves several key barriers to scientific understanding of the Warm Arctic-Cold Eurasia pattern. First, we infer causal effects without relying on targeted perturbation experiments, enabling direct model-observation comparison. Second, we utilize the efficiency of our method to analyze a fully coupled large ensemble, separating forced responses from internal variability. Finally, we calculate transient responses to the time history of causal drivers, and in doing so reveal the dependence of Arctic-midlatitude connections on different mean climate states.

2. Methods

We quantify Arctic-midlatitude linkages in observations provided by the NASA Global Modeling and Assimilation Office's latest reanalysis product, MERRA-2 (Gelaro et al. 2017). These linkages are compared with fully coupled model output from the CESM2 Large Ensemble (CESM2-LE, Rodgers et al. 2021), which simulates historical climate change in one hundred ensemble members. By applying our investigation across ensemble members, we can analyze forced climate responses (the ensemble mean), internal variability (the ensemble spread), and the degree to which observed historical trends lie within simulated internal variability. Lastly, we compare MERRA-2 reanalysis with the latest European Center for Medium Range Weather Forecasting (ECMWF) reanalysis, ERA-5 (Hersbach et al. 2019), ensuring that our results are robust to the choice of observational data source.

2.1. Regional Trend Assessment

Following Blackport and Screen (2020), our analysis focuses on the 1988-2012 period, known as a pronounced interval of wintertime Eurasian cooling. In Section 3.1, linear trends in 1988-2012 winter (DJF) climate are calculated with an ordinary least squares approach for five spatially aggregated climate indices associated with the Warm Arctic-Cold Eurasia pattern: Barents-Kara sea-ice extent (65°-85°N,10°-90°E), Eurasia near-surface air temperature (T_{2m}, 40°-60°N, 60°-120°E), Ural sea-level pressure (55°-70°N,40°-90°E), stratospheric polar vortex strength ($[u_{10}]$, 60°-80°N), and the phase of the North Atlantic Oscillation (NAO). The first four variables follow the regional definitions used in Blackport and Screen (2021) and are shown with black polygons in Fig. 1. The NAO time series is calculated by projecting sea-level pressure anomalies in each gridcell onto the the first empirical orthogonal function mode of December–March sea-level pressure for the 65°-85°N,85°W-60°E domain (Peings 2019). The NAO is a prominent large-scale mode of climate variability in our region of interest, tracking the strength of the sea-level pressure dipole associated with Icelandic Low and the Azores High. For each variable, we test whether trends are significantly different from zero (5% level) using a two-sided t-test.

In Section 3.3, trends in Barents-Kara sea ice and Central Eurasian temperature are calculated in a similar manner, using weekly December-March anomalies. Due to differences in the temporal resolution and seasonal range of these time series, the trend magnitudes differ slightly from those referenced in Section 3.1 for the same regions.

2.2. PCMCI Algorithm

The PCMCI algorithm (Runge et al. 2019) is applied in Section 3.2 to identify robust causal relationships underlying the Warm Arctic-Cold Eurasia Pattern. The algorithm is characterized by a two-step causal discovery procedure: the PC-stable causality test (named after its creators, Peter Spirtes and Clark Glymour; Spirtes et al. 2000), followed by the Momentary Conditional Independence (MCI) test (Runge et al. 2019). Section 2.2.1 describes the first step, and Section 2.2.2 describes the second step. Statistical significance assessment in PCMCI is described in Section 2.2.3. The Tigramite coding and graphics package for PCMCI (`https://jakobrunge.github.io/tigramite/`) is used to produce the data discussed in Section 3.2 and the causal network visualizations in Fig. 2.

One hundred distinct causal networks are constructed for each CESM2-LE ensemble member (historical simulations) and MERRA-2 reanalysis (observations), using five input time series spanning 1988-2012. To address signal intermittency in the short observational record, we apply a bootstrapping procedure (Siew et al. 2020) that generates one hundred observation-based time series samples to accompany the one hundred CESM2 ensemble members. The MERRA-2 bootstrap samples consist of twenty-four randomly selected years from the reanalysis period (with replacement). Before input to PCMCI, daily time series variables are linearly detrended and standardized by subtracting the mean and dividing by the standard deviation for each day in the annual cycle. Then, the daily anomalies are downsampled to weekly averages.

2.2.1. PC-Stable PC-stable identifies a set of potential causal drivers for each variable, x, in the causal network using a series of iterative correlation calculations. In iteration one, every possible time-lagged linear autocorrelation and cross-correlation, from τ=1 to $\tau = \tau_{\text{max}}$ (twelve weeks), is calculated as:

$$\rho(X_i(t-\tau), X_j(t)) \tag{1}$$

where ρ is the Pearson correlation coefficient, τ is a time lag (weeks), and $X_i(t-\tau)$ are lagged time series with a potential causal influence on $X_j(t)$. Contemporaneous links are not considered. If the value of ρ is found to be not significantly different from zero, $X_i(t-\tau)$ is eliminated from the set of potential causal drivers of $X_j(t)$.

In iteration two, the correlations are re-calculated for the remaining potential drivers as:

$$\rho(X_i(t-\tau), X_j(t))|Z_1) \tag{2}$$

where $Z_1 \neq X_i(t-\tau)$ is the auto or cross-link with the strongest unconditional correlation with $X_j(t)$ in Eqn. 1. The vertical line in Eqn. 2 denotes removing the linear influence of Z_1 from both $X_i(t-\tau)$ and $X_j(t)$ and testing the correlation between their residuals. If Z_1 makes the formerly significant link insignificant, the two variables are said to be conditionally independent, and the link is subsequently removed. This process is repeated over n iterations by adding an increasingly stringent number of conditions, Z_2, Z_3, ... , Z_n to the partial correlation tests until no more links can be removed. The PC-algorithm finishes when it converges to a final set of significant links for each variable, which are defined as the "parents" of each variable: $\mathbf{P}(X_j(t))$.

2.2.2. MCI In the second step of the PCMCI algorithm, the MCI test, the full set of lagged autocorrelations and cross-correlations is calculated a final time, using each variable's parents identified in step one as a single conditioning set:

$$\rho(X_i(t-\tau), X_j(t)|\hat{\mathbf{P}}(X_j(t)), \mathbf{P}(X_i(t-\tau))) \tag{3}$$

where $\hat{\mathbf{P}}(X_j(t))$ are the parents of , $X_j(t)$, excluding $X_i(t-\tau)$, and $\mathbf{P}(X_i(t-\tau)))$ are the parents of $X_i(t-\tau)$. The final set of significant links identified in Eqn. 3 are considered the causes of $X_j(t)$, shown for our system of interest in Fig. 2. This designation is based on the causal Markov condition, which states that X_j is independent of all network variables, except X_j's effects, when conditioned on the causes of X_j (Spirtes et al. 2000).

2.2.3. Significance When assessing linear partial correlation strength (e.g., ρ in Eqns. 1-3), we apply a statistical significance threshold, α, to define the range of acceptable p-values for rejecting the null hypothesis of conditional independence. For our test statistic, α thus represents the probability of a Type 1 error, or the expected rate of false positives. However, iterative causal discovery procedures, such as PC-stable, consist of repetitive testing, which may affect the rate of false positives. In numerical validations of PC-stable, for instance, combined false positive rates are typically much lower than those expected from individual significance tests (Runge 2018). The two-step approach of PCMCI serves to address this repetitive testing issue.

First, PC-stable is conducted for a range of large significance thresholds, where hyperparameter $\alpha = [0.1, 0.2, 0.3, 0.4]$. The significant links identified for each value of α are used to estimate linear lagged regression models, which are compared using the Akaike Information Criterion (AIC). The choice of α associated with the minimum AIC value defines the parents of each variable in PC-stable, $\mathbf{P}(X_j(t))$ (Eqns. 1-2). In the subsequent MCI tests, the constant conditioning set of Eqn. 3 is able to avoid the sequential testing issue of PC-stable, and α can return to a stricter, robustly defined threshold, with α=0.01 (1%) used in this study. Finally, the p-value of every assessed link in the MCI tests is adjusted using the Hochberg–Benjamini false discovery rate (FDR) control (Benjamini and Hochberg 1995). The adjusted p-values are given by:

$$q = min(P\frac{m}{r}, 1) \tag{4}$$

where P is the individual link p-value, m is the number of conditional independence tests applied with Eqn. 3, and r is the ascending-order rank of P among all tests. Ultimately, the significance assessment procedure in PCMCI allows it to achieve high detection power, while simultaneously controlling for the number of false positives (Runge et al. 2019).

2.3. Climate Response Functions

A climate response function can be regarded as a quasi-Green's function, $G(\tau)$, which we use to describe the hypothetical response of temperature and sea ice to a $+1\sigma$ step increase in Ural sea-level pressure at time lag τ (Section 3.3). In this study, the calculation of $G(\tau)$ takes place within a causal inference framework, as introduced in Pearl (2013) and Runge et al. (2015), and corresponds to the "total causal effect" metric described in Kaufman and Feldl (2022).

After uncovering each variable's causal predictors with PCMCI, we quantify causal effects using a vector autoregressive (VAR) model:

$$\mathbf{X}(t) = \sum_{\tau=1}^{\tau_{\max}} \Phi(\tau)\mathbf{X}(t-\tau) + \epsilon_t \tag{5}$$

where $\mathbf{X}$ is a vector of shape (N, t) containing time series for N variables, Φ is a standardized regression coefficient matrix of shape $(N, N, \tau_{\max})$, and ϵ_t is a (N, t) vector of white noise errors. An individual regression coefficient, or link coefficient, $\Phi_{j,i}(\tau)$, indicates the expected change in variable $X_j(t)$ caused by a hypothetical 1σ perturbation in $X_i(t-\tau)$ with all other variables held constant. $\tau_{\max}$ refers to the time domain over which link coefficients are added. Importantly, $\Phi_{j,i}(\tau) = 0$ unless $X_i(t-\tau)$ causes $X_j(t)$, as determined by PCMCI. This key feature of matrix Φ frees the VAR model from having to fit negligible parameters, thus allowing it to accommodate a large number of variables and time lags.

The causal inference framework also allows us to account for coupled interactions modulating the responses to a step change in a causal network variable. The full set of climate response functions $\mathbf{G}(\tau)$ for a causal network is found by iteratively computing matrix products of the coefficient matrices $\Phi(\tau)$ in Eqn. 5:

$$\mathbf{G}(\tau) = \sum_{s=1}^{\tau} \Phi(s)\mathbf{G}(\tau - s). \tag{6}$$

Note that Eqn. 6 shown above is equivalent to Eqn. 6 in Kaufman and Feldl (2022), except total causal effect $\mathbf{TCE}(\tau)$ is redefined as $\mathbf{G}(\tau)$ to emphasize its mathematical resemblance to Green's functions, which is relevant for the linear convolutions conducted in Section 3.3. $\mathbf{G}(\tau)$ can be further decomposed into Green's functions for individual pairs of driver and response variables, which is accomplished by restricting Φ to the specific causal pathways that connect them. In Section 3.3, we isolate Green's functions for the Eurasian temperature and Barents-Kara sea-ice response to a Ural sea-level pressure anomaly.

3. Results

3.1. Divergent Midlatitude Trends

Regional trends associated with the Warm Arctic-Cold Eurasia pattern are shown in Fig. 1 for boreal winter (DJF), highlighting key similarities and differences between MERRA-2 and CESM2-LE. Observed and modeled trends both exhibit Arctic sea-ice loss in marginal ice zones (Fig. 1a,b) and Arctic-amplified warming below 850 hPa (red contours, Fig. 1e,f). The Barents-Kara Sea experiences the largest regional sea-ice loss in both cases, featuring an observed trend of -1.5 $\times$ 10^5 km^2 per decade and smaller simulated trends of -0.74 $\pm$0.59 $\times$ 10^5 km^2 per decade. Beyond Arctic surface climate, large model-observation discrepancies become apparent. Over central Eurasia (solid black polygon, Fig. 1c,d), observations feature a significant cooling trend of -1.3 °C per decade (Fig. 1c), whereas simulations feature near-surface warming throughout the Northern Hemisphere (Fig. 1d). Over the Ural mountain region (dashed black polygon, Fig. 1c,d) observations feature a prominent positive sea-level pressure trend of 5.0 hPa per decade (green contours, Fig. 1c), whereas simulations feature a range of positive and negative sea-level pressure trends, with negligible changes in the ensemble mean (-0.27±1.4 hPa per decade, Fig. 1d). In the stratosphere, observations indicate a secondary polar warming peak aloft and a corresponding weakening of the polar vortex, where polar-cap averaged $[u_{10}]$ decreases by -4.7 m s^{-1} per decade (Fig. 1e). Neither of these features are apparent in the CESM2-LE ensemble mean, where circulation trends associated with the Warm Arctic-Cold Eurasia pattern are absent (Fig. 1f). Fig. S1 shows the trends in winter climate in ERA-5 reanalysis.

3.2. A Robust Causal Driver of the Warm Arctic-Cold Eurasia Pattern

For reanalysis and each CESM2-LE ensemble member, we construct causal networks from the five aforementioned 1988-2012 time series (Fig. 2 and Fig. S2), which highlight drivers of the Warm Arctic-Cold Eurasia pattern. The causal links identified by the PCMCI algorithm are given by the lagged, linear correlations that remain significant after controlling for indirect mediators, common drivers, and autocorrelation (memory). We evaluate relationships amongst detrended anomalies at lags of one to twelve weeks, accommodating both the shorter timescale of atmospheric variability and the longer timescale of sea-ice variability. Lastly, we restrict correlation calculations to the months of September-March, encompassing the seasons of maximum Arctic sea-ice loss (early fall) and the active Warm Arctic-Cold Eurasia Pattern (winter). This masking step accounts for the seasonal dependence of sea-ice variability and any causal effects associated with it.

The causal networks identify two significant causal relationships as remarkably robust in both models and observations, appearing in 99-100% of MERRA-2 bootstrap samples (Fig. 2a) and CESM2-LE ensemble members (Fig. 2b). Both links are associated with anomalies in Ural sea-level pressure (Node 2.), which predict opposite-signed anomalies in both Barents-Kara sea-ice extent (2. $\rightarrow$ 1.) and central Eurasia T_{2m} (2. $\rightarrow$ 3.). The causal links are strongest at a lag of one week, where the average partial correlation coefficient ($\overline{r}$, link color) between Ural sea-level pressure and Barents-Kara sea-ice is -0.35 in both MERRA-2 and CESM2-LE. The lag-1 partial correlations are similar between Ural sea-level pressure and central Eurasia T_{2m}, with an $\overline{r}$ of -0.33 and -0.32 for MERRA-2 and CESM2-LE, respectively. Interpreted physically, these two robust links indicate that Ural blocking events (positive sea-level pressure anomaly) can drive both sea-ice loss (Warm Arctic, 2. $\rightarrow$ 1.) and midlatitude cooling (Cold Eurasia, 2. $\rightarrow$ 3.) on weekly timescales.

Interestingly, atmospheric responses to Barents-Kara sea-ice anomalies are comparatively weak and intermittent. In MERRA-2, Ural blocking anomalies are caused by Barents-Kara sea-ice loss (1. $\rightarrow$ 2.) at lags of seven to ten weeks ($\overline{r}$ = -0.21 at lag-10), but this relationship is only detected in 37% of MERRA-2 bootstrap samples. Barents-Kara sea-ice loss also predicts a negative NAO phase in MERRA-2 (1. $\rightarrow$ 4.), but this signal is similarly intermittent, being featured in 42% of MERRA-2

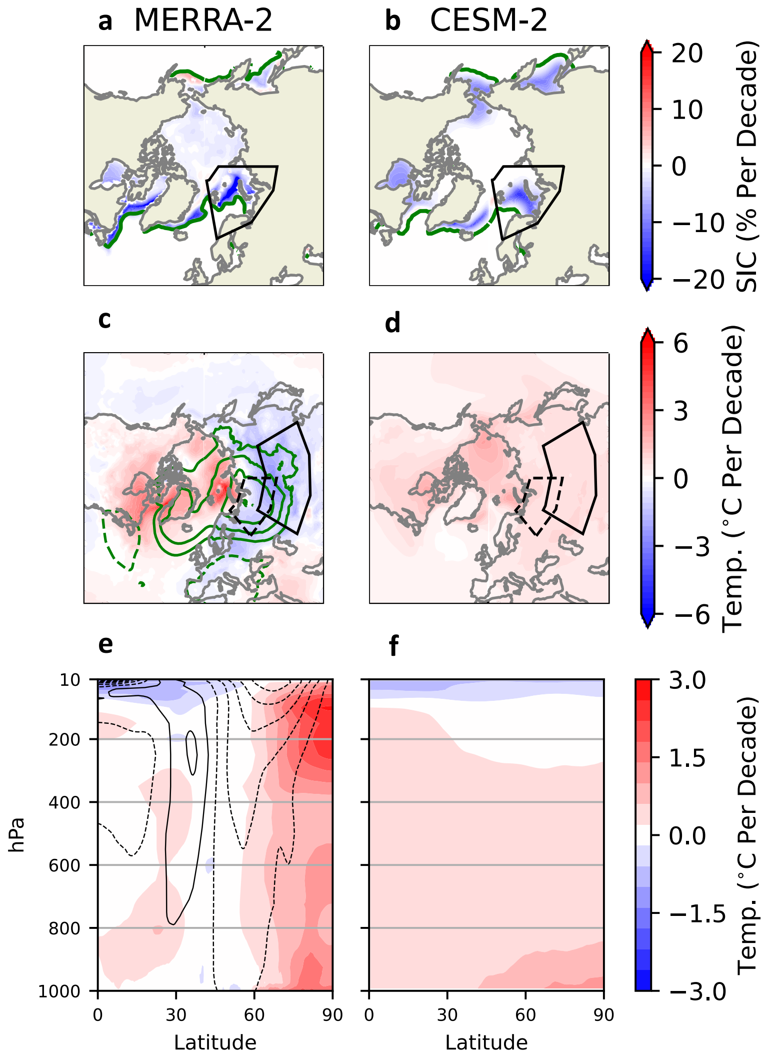

Figure 1: **a-b**, Trends in Arctic sea-ice concentration (red and blue contours, % per decade) and the climatological DJF sea-ice concentration over the 1988-2012 time period (5% contour, green). **c-d**, Trends in near-surface air temperature (red and blue contours, °C per decade) and sea-level pressure (green contours, hPa per decade), displayed in intervals of 1.5 hPa from -6 to 6 (zero omitted), with dashed and solid contours indicating negative and positive values, respectively. **e-f**, Vertical profiles of zonal mean trends in temperature (red and blue contours, °C per decade) and zonal wind (black contours, m s^{-1} per decade), displayed in intervals of 1 m s^{-1} from -7.5 to 7.5, with dashed and solid contours shown as in **c-d**. The dashed black polygon indicates the Ural blocking region (**c-d**); the solid black polygons indicate the Barents-Kara Sea region (**a-b**) and central Eurasia region (**c-d**). The statistical significance and ensemble spread in spatially aggregated trends are shown in Fig. S3.

bootstrap samples. Neither causal link is present in CESM2-LE. Furthermore, while causal networks highlight slackened stratospheric winds as a response to anomalously meridional flow in the troposphere (2. $\rightarrow$ 5., Fig. 2a,b; 4. $\rightarrow$ 5., Fig. 2a), direct causal links between the polar vortex and Barents-Kara sea-ice extent are nearly non-existent (1. $\rightarrow$ 5.). These weak atmospheric responses to sea-ice loss were also found in sensitivity tests with monthly time stepping intervals, as well as when changing the averaging region used to define the Barents-Kara Sea (not shown). The reanalysis results are consistent with a similar causal network analysis of Kretschmer et al. (2016), who identified two-way causality between Barents-Kara sea-ice extent and Ural sea-level pressure in observations at the sub-seasonal time scale. However, we additionally find that the causal effect of sea ice is intermittent (based on bootstrap resampling) and not captured in corresponding historical simulations. This difference is notable given the large discrepancy in Ural sea-level pressure trends in CESM2-LE and MERRA-2 (Fig. 1c,d; Fig. S3), which we examine further in the following section.

Our causal network analysis can thus be summarized as follows. Positive Ural sea-level pressure anomalies (Ural blocking) are a robust atmospheric driver of the Warm Arctic-Cold Eurasia pattern in both observations (Fig. 2a) and models (Fig. 2b). In observations, a smaller subset of time samples suggest a two-way interaction (Fig. 2a), whereby Ural blocking mediates a Eurasian cooling response to sea-ice loss. These results indicate that Ural blocking variability is the most likely source of the model-observation discrepancy in historical Eurasian cooling (Fig. 1c,d).

3.3. The Transient Response to Ural Blocking

We next assess how historical trends in Barents-Kara sea ice and Eurasian temperature depend on the time history of Ural blocking. This component of our analysis advances the use of linear convolution theory, whereby the transient response of variable Y to forcing F can be estimated as the convolution of a Green's Function $G(\tau)$ with the time history of the forcing, assuming the response is linear:

$$\hat{Y}(t) \approx \sum_{\tau=1}^{\tau_{\max}} G(\tau)F(t-\tau)\Delta\tau. \tag{7}$$

For our application, Green's Function $G(\tau)$ is the step-response of Y to a one standard deviation perturbation in Ural sea-level pressure at time lag τ (weeks), and $\hat{Y}(t)$ is the transient response to the time history of Ural sea-level pressure $F(t-\tau)$. When derived from model perturbation experiments or lagged linear regressions, $G(\tau)$ has been described as a climate response function (Marshall et al. 2014; Kostov et al. 2018; Rye et al. 2020). Here, we derive $G(\tau)$ from our causal inference framework, where it represents the total causal effect of a hypothetical $+1\sigma$ anomaly in Ural sea-level pressure.

The $G(\tau)$ step responses to Ural sea-level pressure are shown in Fig. 3 for Eurasia T_{2m} (Fig. 3a) and Barents-Kara sea ice (Fig. 3b). The Eurasian cooling response to a

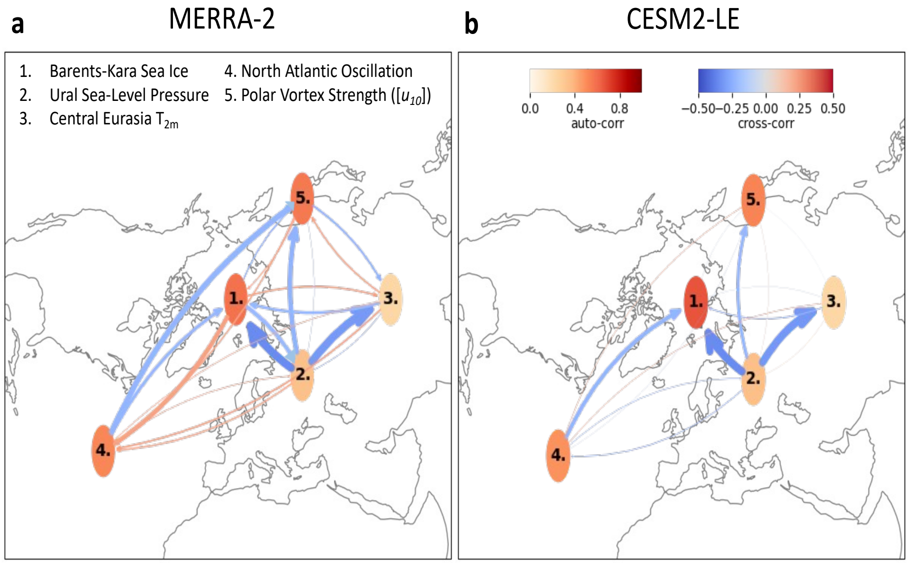

Figure 2: Time-lagged causal links between Barents-Kara Sea ice, Ural sea-level pressure, Central Eurasia 2m air temperature, NAO Phase, and polar vortex strength ($[\mathbf{u_{10}}]$). Potential causal relationships are evaluated by the PCMCI algorithm over lags of one to twelve weeks for the 1988-2012 period in the months of September-March. Arrows denote the direction and strength of causal links deemed significant at the α=.01 level. Arrow thickness indicates the frequency of link detection among the one hundred bootstrap samples from MERRA-2 (**a**) and one hundred CESM2-LE ensemble members (**b**), with the thickest arrows appearing in 99-100% of samples. Arrow color indicates the average partial correlation coefficient at the time lag with the largest signal; specific lags associated with each link are described in Section 3. Node color indicates the first-order autocorrelation coefficient associated with each variable.

Ural blocking anomaly peaks at $\tau = 1$ week, with values of -3.1 °C for MERRA-2 and -2.3 °C for the CESM2-LE ensemble mean, before gradually decaying to zero by $\tau =$ 7 weeks. Barents-Kara sea ice also decreases in response to Ural blocking, with a $\tau =$ 2 weeks peak of -0.28 $\times$ 10^5 km^2 in MERRA-2 and a $\tau = 1$ week peak of -0.24 $\times$ 10^5 km^2 for the CESM2-LE ensemble mean. In both datasets, the sea-ice response persists over a longer time period than the temperature response, consistent with the longer decorrelation length scale of sea-ice anomalies (node color, Fig. 2). The MERRA-2 responses to a step increase in Ural sea-level pressure are larger than the CESM2-LE ensemble mean, but still well within the ensemble spread, indicating a qualitative similarity (compare black and blue curves, Fig. 3a,b).

Despite the similar step responses, observed and simulated Ural sea-level pressure time histories (Fig. 3c) exhibit large differences. Over the entire historical period (1920-2012), there is a 48% chance of observing a positive 24-year trend in wintertime Ural sea-level pressure in CESM2-LE (blue histogram, Fig. 3c), but only a 0.14% chance of observing a positive trend as large as the 5.0 hPa per decade trend seen in 1988-

2012 observations (vertical dashed line, Fig. 3c). This low probability suggests an inherent inability of CESM2 to accurately simulate the observed sea-level pressure trend. Additionally, even if models and observations have a similar sensitivity to Ural blocking, their transient response to the Ural blocking time histories can be quite different. This difference will become apparent when the Green's functions (Fig. 3a,b) are convolved with the Ural blocking time histories (Fig. 3c).

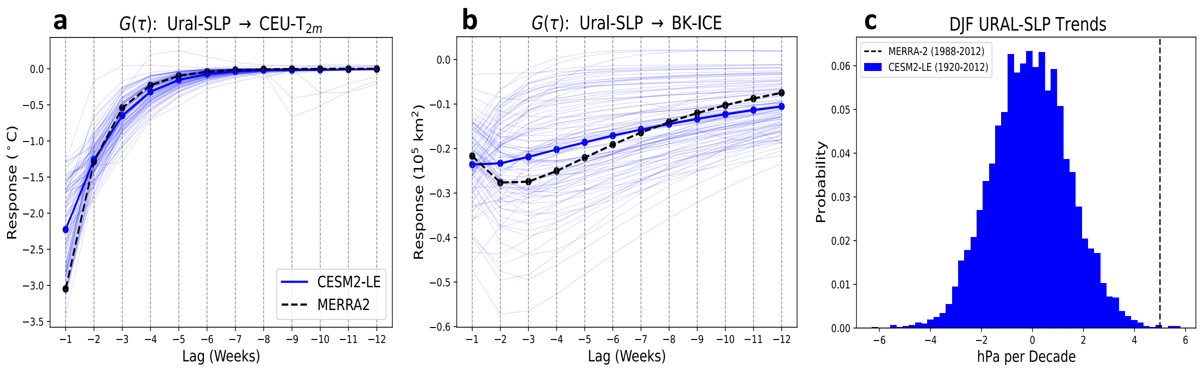

Figure 3: **a-b** $G(\tau)$, the estimated response of Central Eurasia T_{2m} and Barents-Kara sea ice to a hypothetical $+1\sigma$ step increase in Ural sea-level pressure at lags of one to twelve weeks. Response functions are shown with thin blue lines for one hundred individual CESM2-LE ensemble members, thick blue lines for the CESM2-LE ensemble mean, and dashed black lines for MERRA-2 reanalysis. **c** Probability distribution of 24-year trends in winter (DJF) Ural sea-level pressure (hPa per decade) over the entire historical period in CESM2-LE (1920-2012, blue histogram). The 1988-2012 Ural sea-level pressure trend from MERRA-2 is shown with a dashed vertical line for comparison.

Applying Eqn. 7 to the quantities in Fig. 3 yields the transient response of Eurasian temperature and Barents-Kara sea ice to the time history of Ural blocking (Fig. 4). As previously noted, the observed winter trend in Central Eurasia temperature is one of cooling (-1.0 °C per decade, black line, Fig. 4a), and the ensemble mean simulated trend is one of warming (0.80 °C per decade, thick blue line, Fig. 4a). These divergent midlatitude trends can be reconciled by distinct transient temperature responses to Ural blocking. Specifically, in observations, Eurasia cools strongly, by -1.9 °C per decade, in response to Ural blocking (black curve, Fig. 4b). By contrast, the wide range of Ural sea-level pressure trends in CESM2-LE (Fig. 3c) produce both negative and positive temperature responses (thin blue curves, Fig. 4b), with a weak positive response in the ensemble mean (0.13 °C per decade, thick blue curve, Fig. 4b). Once the transient effects of Ural blocking are removed, both observed and simulated Eurasian temperature trends feature a remarkably similar warming signal: 0.89 and 0.67 °C per decade in MERRA-2 and the CESM2-LE ensemble mean, respectively (Fig. 4c). We interpret these warming signals as the trend due to anthropogenic forcing, which, for observations, was masked in Fig. 4a by the abnormally large Ural sea-level pressure trend.

Unlike Eurasian temperature, models and observations agree that 1988-2012 winter sea-ice retreat occurred in the Barents-Kara sea, as previously shown in Fig. 1a,b. However, the observed December-March trend in sea-ice extent (-1.4 $\times$ 10^5 km^2 per decade, black curve, Fig. 4d) is larger than in the CESM2-LE ensemble mean (-0.67 $\times$ 10^5 km^2 per decade, blue curves, Fig. 4d). Here too, accounting for the transient response to Ural blocking helps to bring models and observations into agreement. MERRA-2 features the largest transient response to Ural blocking (-0.74 $\times$ 10^5 km^2 per decade, Fig. 4e), which explains half of the observed 1988-2012 winter trend. CESM2-LE has a negligible transient response to Ural blocking in the ensemble mean. When the effect of Ural blocking is removed, observed and simulated trends in sea-ice loss are similar (-0.65 and -0.72 $\times$ 10^5 km^2 per decade; Fig. 4f). This similarity implies that the larger sea-ice loss trend in observations (Fig. 4d) can be attributed to the Ural blocking trend (Fig. 4e). In other words, the large positive Ural sea-level pressure trend in MERRA-2 (Fig. 3c) amplified observed 1988-2012 Barents-Kara sea-ice loss.

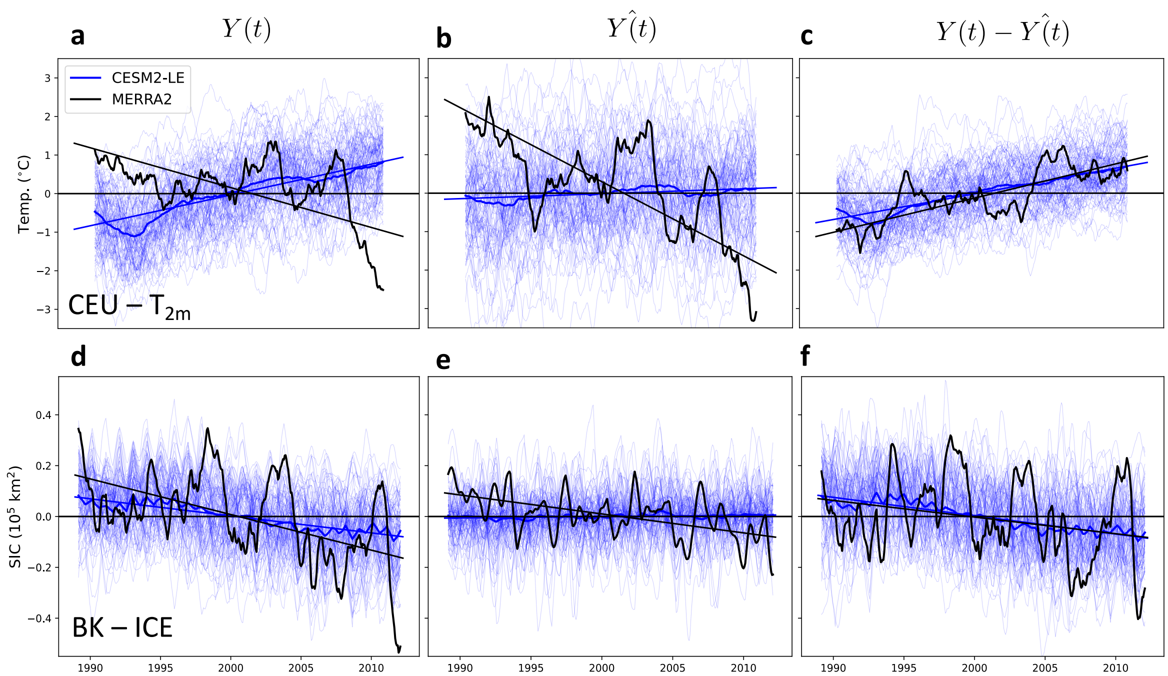

Figure 4: **a-c** Time series of Central Eurasia T$_{2m}$ in CESM2-LE (blue) and MERRA-2 (black), shown as weekly December-March anomalies relative to the 1988-2012 climatology. The left column ($Y(t)$, **a**) shows observed and simulated trends, while the middle column ($\hat{Y(t)}$, **b**) shows the transient response to the time history of Ural sea-level pressure. The right column shows the difference ($Y(t)$ - $\hat{Y(t)}$, **c**), representing the temperature trends with the effects of Ural blocking variability removed. **d-f** The same as **a-c**, but for 1988-2012 time series of Barents-Kara Sea Ice. For ease of visualization, a 12-month rolling mean is applied to the weekly temperature anomalies (**a-c**) and a 2-month rolling mean is applied to the weekly sea-ice anomalies (**d-f**).

It is important to note that the transient Eurasian temperature responses to Ural blocking ($\hat{Y(t)}$, Fig. 4b) are initially calculated assuming that the atmospheric forcing is independent from background sea-ice trends. This assumption is consistent with the causal links identified in CESM2 historical simulations (Fig. 2b), which only indicate a causal effect of Ural blocking on Barents-Kara sea-ice extent, not vice-versa. However, observations feature bi-directional causality between sea ice and Ural sea-level pressure (Fig. 2a). Accordingly, we further calculate the transient response of Ural sea-level pressure to sea-ice changes in MERRA-2, and subtract it from the sea-level pressure forcing time series, $F(t)$. This adjustment, shown with the dotted curve in Fig. 5a, reveals that as much as 80% of the observed Ural sea-level pressure trend is explained by the causal effect of sea-ice loss, which is only found in observations. The transient Eurasian temperature response to Ural sea-level pressure in MERRA-2 can thus be calculated for both the cooling response to the total trend (solid black curve, Fig. 4b, Fig. 5b) and the smaller cooling response to the forcing independent of sea-ice changes (dotted curve, Fig. 5b). Comparing the two curves shows that the majority of the total cooling response in MERRA-2 is explained by the indirect effect of sea-ice loss. The smaller, remaining cooling that is independent of sea-ice loss (-.40 °C per decade) is within the ensemble spread of simulated CESM2-LE responses to Ural sea-level pressure (.13 ± .58 °C per decade, blue curves, Fig. 4b) and thus consistent with internal variability.

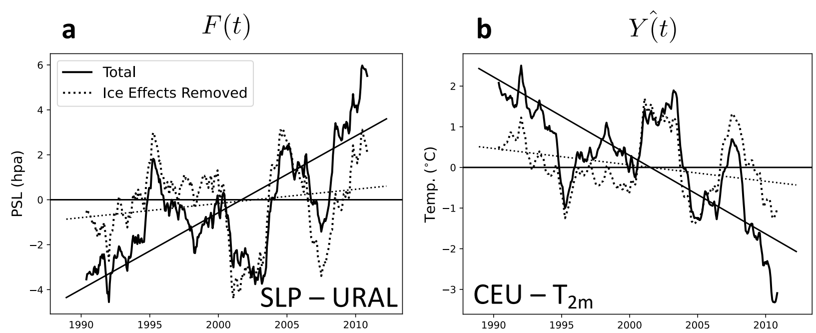

Figure 5: Sea-ice impacts on the transient temperature response to Ural blocking variability in MERRA-2 reanalysis. Time series of Ural sea-level pressure ($F(t)$, **a**) and Central Eurasia T_{2m} ($\hat{Y(t)}$, **b**), displayed as anomalies as in Fig. 4, but for MERRA-2 reanalysis only. The solid curve in **a** (Total) is the observed Ural sea-level pressure trend and the dotted curve is the trend that remains after subtracting the causal effect of 1988-2012 Barents-Kara sea-ice loss. The corresponding curves in **b** are transient responses of Central Eurasia T_{2m} to each forcing time series $F(t)$. Note that the solid curve in **b** is identical to the solid black curve in Fig. 4b.

4. Summary and Discussion

We use a causal inference algorithm to identify a common atmospheric driver of the Warm Arctic-Cold Eurasia Pattern: Both Barents-Kara sea-ice loss and Central Eurasian cooling are caused by positive anomalies in Ural sea-level pressure on weekly timescales. Observed sea-ice loss itself also intermittently affects Ural sea-level pressure (a two-way interaction), but the signal associated with this causal pathway is absent in a set of fully coupled large ensemble simulations. Second, we show that the observed positive trend in Ural sea-level pressure was abnormally large between the winters of 1988 and 2012, lying outside the distribution of simulated variability. The transient response to this Ural blocking trend produced a midlatitude cooling tendency that temporarily masked the long-term warming trend, whilst simultaneously amplifying the rate of anthropogenic sea-ice loss. These results highlight the importance of both anthropogenic sea-ice loss and atmospheric variability for assessing the likelihood of opposing temperature trends in the Arctic and midlatitudes.

While we consider our analysis and findings to be robust, there are potential uncertainties arising from statistical choices and assumptions that should be acknowledged. First, our analysis focuses on the 1988-2012 time period, when particularly large Eurasian cooling was observed. This approach has been used in prior studies (Cohen et al. 2012; Overland et al. 2015; Outten et al. 2023), but caution should still be used when extrapolating our conclusions to different time periods. Second, our study uses a single climate model, the CESM2 large ensemble, even though the strength of Arctic-midlatitude connections likely varies across coupled models (Smith et al. 2022). Despite this caveat, our use of a large ensemble offers its own advantage of enabling the separation of forced responses from internal variability. Finally, the results of causal inference analysis can be sensitive to the choice of the variables considered in the causal network and the assumption of linear relationships among them. We are encouraged by the qualitative similarity between the Arctic-midlatitude connections identified in MERRA-2 reanalysis (our study) and the connections identified in ERA-interim reanalysis by Kretschmer et al. (2016), despite differences in the input variables considered. Furthermore, we believe linearity provides a good first-order approximation of causal relationships over the short time periods considered here.

Our analysis builds upon the prior causal inference studies that highlight intermittent, two-way interactions between Barents-Kara sea-ice extent and midlatitude circulation (Kretschmer et al. 2016; Kretschmer et al. 2020; Siew et al. 2020). In spite of this intermittency, we identify an atmospheric driver of the Warm Arctic-Cold Eurasia pattern that is robust across climate states in both models and observations. This key role of Ural blocking is consistent with the mechanisms identified in a variety of targeted model experiments. For instance, Ural blocking anomalies imposed in an otherwise stable climate produce temperature anomalies consistent with the Warm Arctic-Cold Eurasia pattern, as well as a weakened stratospheric polar vortex (Peings 2019) . This circulation pattern shapes the midlatitude storm track in a manner that favors moist intrusions into the Barents-Kara sea, where anomalous poleward eddy fluxes lead to sea-ice melt in winter (Woods and Caballero 2016; Luo et al. 2017). Meanwhile, Ural blocking simultaneously promotes cold-air outbreaks along its eastern flank, leading to cooling over Eurasia. Our causal networks show that Ural blocking impacts also extend to the upper atmosphere, weakening stratospheric winds, with minimal contributions from sea-ice loss. Unlike the bottom heavy warming signal associated with sea-ice loss, moist energy transport from lower latitudes, including intrusions promoted by Ural blocking, tend to cause more vertically extensive Arctic warming (Feldl et al. 2020; Kaufman and Feldl 2022) and a weakened polar vortex (Cardinale et al. 2021). Consistent with this dynamical pathway, Eurasian cooling does occur in model experiments with deep tropospheric warming in the Arctic (He et al. 2020; Labe et al. 2020).

Though Ural blocking variability is clearly central in driving Warm Arctic-Cold Eurasia Pattern, internal variability may not be the dominant cause of the observed Eurasian cooling period; we also identify an important role for sea-ice loss in modulating the impacts of Ural blocking in MERRA-2 reanalysis. The mechanism for this secondary effect is not immediately apparent in our causal networks, but a recent study has suggested that low sea-ice conditions result in more persistent polar vortex warming after a Ural blocking event, which feeds back onto atmospheric conditions in the North Atlantic (Peings et al. 2023). A key priority for future work is to ascertain why this coupling between Barents-Kara sea-ice extent and Ural blocking is not captured in CESM2-LE historical simulations, as demonstrated by our model-observation comparison. One possibility is highlighted by the Polar Amplification Model Intercomparison Project (PAMIP), which found that climate models are systematically biased in their representation of the midlatitude eddy momentum feedback, weakening their simulated circulation response to sea-ice loss (Smith et al. 2022). Since the PAMIP experimental framework focused exclusively on the consequences of Pan-Arctic sea-ice loss, it remains unclear how much this bias characterizes the dynamics of the smaller sub-region comprising the Warm Arctic-Cold Eurasia Pattern, and further, regionally targeted investigations are needed. Our causal analysis will provide an essential roadmap for designing these future analyses, bridging the gap between models and observations.

Data Availability

All data sets used in this study are publicly available. The CESM2 large ensemble output is provided at `https://www.cesm.ucar.edu/community-projects/lens2/data-sets`. ERA5 reanalysis is provided at `https://cds.climate.copernicus.eu/#!/home` and MERRA-2 reanalyis is provided at `https://disc.gsfc.nasa.gov/datasets?project=MERRA-2`.

Code Availability

Analysis code can be made available by Z.S.K (`zackkauf@stanford.edu`) upon request.

Acknowledgments

Support for Z.S.K. was provided by the National Science Foundation Graduate Research Fellowship Program under Grant No. (NSF DGE-1842400). N.F. was supported by NSF award AGS-1753034, and C.B. was supported by NSF award AGS-2143550.

References

Barnes, E. A. and J. A. Screen (2015). “The impact of Arctic warming on the midlatitude jet-stream: Can it? Has it? Will it?” In: *Wiley Interdisciplinary Reviews: Climate Change* 6.3, pp. 277–286.

Benjamini, Y. and Y. Hochberg (1995). “Controlling the false discovery rate: a practical and powerful approach to multiple testing”. In: *Journal of the Royal statistical society: series B (Methodological)* 57.1, pp. 289–300.

Blackport, R. and J. A. Screen (2020). “Weakened evidence for mid-latitude impacts of Arctic warming”. In: *Nature Climate Change* 10.12, pp. 1065–1066.

— (2021). “Observed statistical connections overestimate the causal effects of Arctic sea ice changes on midlatitude winter climate”. In: *Journal of Climate* 34.8, pp. 3021–3038.

Boland, E. J., T. J. Bracegirdle, and E. F. Shuckburgh (2017). “Assessment of sea ice-atmosphere links in CMIP5 models”. In: *Climate Dynamics* 49.1, pp. 683–702.

Cardinale, C. J., B. E. Rose, A. L. Lang, and A. Donohoe (2021). “Stratospheric and tropospheric flux contributions to the polar cap energy budgets”. In: *Journal of Climate* 34.11, pp. 4261–4278.

Cohen, J., L. Agel, M. Barlow, C. I. Garfinkel, and I. White (2021). “Linking Arctic variability and change with extreme winter weather in the United States”. In: *Science* 373.6559, pp. 1116–1121.

Cohen, J., X. Zhang, J. Francis, T Jung, R Kwok, J Overland, T. Ballinger, U. Bhatt, H. Chen, D. Coumou, et al. (2020). “Divergent consensuses on Arctic amplification influence on midlatitude severe winter weather”. In: *Nature Climate Change* 10.1, pp. 20–29.

Cohen, J. L., J. C. Furtado, M. A. Barlow, V. A. Alexeev, and J. E. Cherry (2012). “Arctic warming, increasing snow cover and widespread boreal winter cooling”. In: *Environmental Research Letters* 7.1, p. 014007.

Deser, C., L. Sun, R. A. Tomas, and J. Screen (2016). “Does ocean coupling matter for the northern extratropical response to projected Arctic sea ice loss?” In: *Geophysical Research Letters* 43.5, pp. 2149–2157.

Feldl, N., S. Po-Chedley, H. K. Singh, S. Hay, and P. J. Kushner (2020). “Sea ice and atmospheric circulation shape the high-latitude lapse rate feedback”. In: *npj Climate and Atmospheric Science* 3.1, pp. 1–9.

Francis, J. A. and S. J. Vavrus (2012). “Evidence linking Arctic amplification to extreme weather in mid-latitudes”. In: *Geophysical research letters* 39.6.

— (2015). “Evidence for a wavier jet stream in response to rapid Arctic warming”. In: *Environmental Research Letters* 10.1, p. 014005.

Gelaro, R., W. McCarty, M. J. Suárez, R. Todling, A. Molod, L. Takacs, C. A. Randles, A. Darmenov, M. G. Bosilovich, R. Reichle, et al. (2017). “The modern-era retrospective analysis for research and applications, version 2 (MERRA-2)”. In: *Journal of climate* 30.14, pp. 5419–5454.

Gong, T. and D. Luo (2017). "Ural blocking as an amplifier of the Arctic sea ice decline in winter". In: *Journal of Climate* 30.7, pp. 2639–2654.

He, S., X. Xu, T. Furevik, and Y. Gao (2020). "Eurasian cooling linked to the vertical distribution of Arctic warming". In: *Geophysical Research Letters* 47.10, e2020GL087212.

Hersbach, H., B. Bell, P. Berrisford, A. Horányi, J. M. Sabater, J. Nicolas, R. Radu, D. Schepers, A. Simmons, C. Soci, et al. (2019). "Global reanalysis: goodbye ERA-Interim, hello ERA5". In: *ECMWF newsletter* 159, pp. 17–24.

Honda, M., J. Inoue, and S. Yamane (2009). "Influence of low Arctic sea-ice minima on anomalously cold Eurasian winters". In: *Geophysical Research Letters* 36.8.

Kaufman, Z. S. and N. Feldl (2022). "Causes of the Arctic's Lower-Tropospheric Warming Structure". In: *Journal of Climate* 35.6, pp. 1983–2002.

Kim, B.-M., S.-W. Son, S.-K. Min, J.-H. Jeong, S.-J. Kim, X. Zhang, T. Shim, and J.-H. Yoon (2014). "Weakening of the stratospheric polar vortex by Arctic sea-ice loss". In: *Nature communications* 5.1, pp. 1–8.

Kostov, Y., D. Ferreira, K. C. Armour, and J. Marshall (2018). "Contributions of greenhouse gas forcing and the Southern Annular Mode to historical Southern Ocean surface temperature trends". In: *Geophysical Research Letters* 45.2, pp. 1086–1097.

Kretschmer, M., D. Coumou, J. F. Donges, and J. Runge (2016). "Using causal effect networks to analyze different Arctic drivers of midlatitude winter circulation". In: *Journal of Climate* 29.11, pp. 4069–4081.

Kretschmer, M., G. Zappa, and T. G. Shepherd (2020). "The role of Barents–Kara sea ice loss in projected polar vortex changes". In: *Weather and Climate Dynamics* 1.2, pp. 715–730.

Labe, Z., Y. Peings, and G. Magnusdottir (2020). "Warm Arctic, cold Siberia pattern: Role of full Arctic amplification versus sea ice loss alone". In: *Geophysical Research Letters* 47.17, e2020GL088583.

Liang, Y.-C., C. Frankignoul, Y.-O. Kwon, G. Gastineau, E. Manzini, G. Danabasoglu, L. Suo, S. Yeager, Y. Gao, J. J. Attema, et al. (2021). "Impacts of Arctic sea ice on cold season atmospheric variability and trends estimated from observations and a multimodel large ensemble". In: *Journal of Climate* 34.20, pp. 8419–8443.

Liang, Y.-c., Y.-O. Kwon, C. Frankignoul, G. Danabasoglu, S. Yeager, A. Cherchi, Y. Gao, G. Gastineau, R. Ghosh, D. Matei, et al. (2020). "Quantification of the Arctic sea ice-driven atmospheric circulation variability in coordinated large ensemble simulations". In: *Geophysical research letters* 47.1, e2019GL085397.

Liu, Z., C. Risi, F. Codron, Z. Jian, Z. Wei, X. He, C. J. Poulsen, Y. Wang, D. Chen, W. Ma, et al. (2022). "Atmospheric forcing dominates winter Barents-Kara sea ice variability on interannual to decadal time scales". In: *Proceedings of the National Academy of Sciences* 119.36, e2120770119.

Luo, B., D. Luo, L. Wu, L. Zhong, and I. Simmonds (2017). “Atmospheric circulation patterns which promote winter Arctic sea ice decline”. In: *Environmental Research Letters* 12.5, p. 054017.

Luo, D., X. Chen, A. Dai, and I. Simmonds (2018). “Changes in atmospheric blocking circulations linked with winter Arctic warming: A new perspective”. In: *Journal of Climate* 31.18, pp. 7661–7678.

Luo, D., X. Chen, J. Overland, I. Simmonds, Y. Wu, and P. Zhang (2019). “Weakened potential vorticity barrier linked to recent winter Arctic sea ice loss and midlatitude cold extremes”. In: *Journal of Climate* 32.14, pp. 4235–4261.

Luo, D., Y. Xiao, Y. Yao, A. Dai, I. Simmonds, and C. L. Franzke (2016). “Impact of Ural blocking on winter warm Arctic–cold Eurasian anomalies. Part I: Blocking-induced amplification”. In: *Journal of Climate* 29.11, pp. 3925–3947.

Marshall, J., K. C. Armour, J. R. Scott, Y. Kostov, U. Hausmann, D. Ferreira, T. G. Shepherd, and C. M. Bitz (2014). “The ocean’s role in polar climate change: asymmetric Arctic and Antarctic responses to greenhouse gas and ozone forcing”. In: *Philosophical Transactions of the Royal Society A: Mathematical, Physical and Engineering Sciences* 372.2019, p. 20130040.

Masson-Delmotte, V., P. Zhai, A. Pirani, S. L. Connors, C. Péan, S. Berger, N. Caud, Y Chen, L Goldfarb, M. Gomis, et al. (2021). “Climate change 2021: the physical science basis”. In: *Contribution of working group I to the sixth assessment report of the intergovernmental panel on climate change* 2.

Mori, M., Y. Kosaka, M. Watanabe, H. Nakamura, and M. Kimoto (2019). “A reconciled estimate of the influence of Arctic sea-ice loss on recent Eurasian cooling”. In: *Nature Climate Change* 9.2, pp. 123–129.

Nishii, K., H. Nakamura, and Y. J. Orsolini (2011). “Geographical dependence observed in blocking high influence on the stratospheric variability through enhancement and suppression of upward planetary-wave propagation”. In: *Journal of Climate* 24.24, pp. 6408–6423.

Ogawa, F., N. Keenlyside, Y. Gao, T. Koenigk, S. Yang, L. Suo, T. Wang, G. Gastineau, T. Nakamura, H. N. Cheung, et al. (2018). “Evaluating impacts of recent Arctic sea ice loss on the northern hemisphere winter climate change”. In: *Geophysical Research Letters* 45.7, pp. 3255–3263.

Outten, S., C. Li, M. P. King, L. Suo, P. Y. Siew, H. Cheung, R. Davy, E. Dunn-Sigouin, T. Furevik, S. He, et al. (2023). “Reconciling conflicting evidence for the cause of the observed early 21st century Eurasian cooling”. In: *Weather and Climate Dynamics* 4.1, pp. 95–114.

Overland, J., J. A. Francis, R. Hall, E. Hanna, S.-J. Kim, and T. Vihma (2015). “The melting Arctic and midlatitude weather patterns: Are they connected?” In: *Journal of Climate* 28.20, pp. 7917–7932.

Pearl, J. (2013). “Linear models: A useful “microscope” for causal analysis”. In: *Journal of Causal Inference* 1.1, pp. 155–170.

Peings, Y (2019). "Ural blocking as a driver of early-winter stratospheric warmings". In: *Geophysical Research Letters* 46.10, pp. 5460–5468.

Peings, Y, P Davini, and G Magnusdottir (2023). "Impact of Ural Blocking on Early Winter Climate Variability Under Different Barents-Kara Sea Ice Conditions". In: *Journal of Geophysical Research: Atmospheres* 128.6, e2022JD036994.

Peings, Y., Z. M. Labe, and G. Magnusdottir (2021). "Are 100 ensemble members enough to capture the remote atmospheric response to +2 °C Arctic sea ice loss?" In: *Journal of Climate* 34.10, pp. 3751–3769.

Rodgers, K. B., S.-S. Lee, N. Rosenbloom, A. Timmermann, G. Danabasoglu, C. Deser, J. Edwards, J.-E. Kim, I. R. Simpson, K. Stein, et al. (2021). "Ubiquity of human-induced changes in climate variability". In: *Earth System Dynamics* 12.4, pp. 1393–1411.

Runge, J. (2018). "Causal network reconstruction from time series: From theoretical assumptions to practical estimation". In: *Chaos: An Interdisciplinary Journal of Nonlinear Science* 28.7, p. 075310.

Runge, J., P. Nowack, M. Kretschmer, S. Flaxman, and D. Sejdinovic (2019). "Detecting and quantifying causal associations in large nonlinear time series datasets". In: *Science advances* 5.11, eaau4996.

Runge, J., V. Petoukhov, J. F. Donges, J. Hlinka, N. Jajcay, M. Vejmelka, D. Hartman, N. Marwan, M. Paluš, and J. Kurths (2015). "Identifying causal gateways and mediators in complex spatio-temporal systems". In: *Nature communications* 6.1, p. 8502.

Rye, C. D., J. Marshall, M. Kelley, G. Russell, L. S. Nazarenko, Y. Kostov, G. A. Schmidt, and J. Hansen (2020). "Antarctic glacial melt as a driver of recent Southern Ocean climate trends". In: *Geophysical Research Letters* 47.11, e2019GL086892.

Screen, J. A. (2017). "Simulated atmospheric response to regional and pan-Arctic sea ice loss". In: *Journal of Climate* 30.11, pp. 3945–3962.

Siew, P. Y. F., C. Li, S. P. Sobolowski, and M. P. King (2020). "Intermittency of Arctic–mid-latitude teleconnections: stratospheric pathway between autumn sea ice and the winter North Atlantic Oscillation". In: *Weather and Climate Dynamics* 1.1, pp. 261–275.

Smith, D. M., R. Eade, M. Andrews, H. Ayres, A Clark, S Chripko, C. Deser, N. Dunstone, J. García-Serrano, G. Gastineau, et al. (2022). "Robust but weak winter atmospheric circulation response to future Arctic sea ice loss". In: *Nature communications* 13.1, p. 727.

Sorokina, S. A., C. Li, J. J. Wettstein, and N. G. Kvamstø (2016). "Observed atmospheric coupling between Barents Sea ice and the warm-Arctic cold-Siberian anomaly pattern". In: *Journal of Climate* 29.2, pp. 495–511.

Spirtes, P., C. N. Glymour, and R. Scheines (2000). *Causation, prediction, and search.*

Sun, L., C. Deser, and R. A. Tomas (2015). "Mechanisms of stratospheric and tropospheric circulation response to projected Arctic sea ice loss". In: *Journal of Climate* 28.19, pp. 7824–7845.

Sun, L., J. Perlwitz, and M. Hoerling (2016). "What caused the recent "Warm Arctic, Cold Continents" trend pattern in winter temperatures?" In: *Geophysical Research Letters* 43.10, pp. 5345–5352.

Taylor, P. C., R. C. Boeke, L. N. Boisvert, N. Feldl, M. Henry, Y. Huang, P. Langen, W. Liu, F. Pithan, S. Sejas, et al. (2021). "Process drivers, inter-model spread, and the path forward: A review of amplified Arctic warming". In.

Tyrlis, E., E. Manzini, J. Bader, J. Ukita, H. Nakamura, and D. Matei (2019). "Ural blocking driving extreme Arctic sea ice loss, cold Eurasia, and stratospheric vortex weakening in autumn and early winter 2016–2017". In: *Journal of Geophysical Research: Atmospheres* 124.21, pp. 11313–11329.

Woods, C. and R. Caballero (2016). "The role of moist intrusions in winter Arctic warming and sea ice decline". In: *Journal of Climate* 29.12, pp. 4473–4485.

Xie, Y., G. Wu, Y. Liu, and J. Huang (2020). "Eurasian cooling linked with Arctic warming: Insights from PV dynamics". In: *Journal of Climate* 33.7, pp. 2627–2644.

Yao, Y., D. Luo, A. Dai, and I. Simmonds (2017). "Increased quasi stationarity and persistence of winter Ural blocking and Eurasian extreme cold events in response to Arctic warming. Part I: Insights from observational analyses". In: *Journal of Climate* 30.10, pp. 3549–3568.